Investigation of Mn Single and Co-Doping in Thermoelectric CoSb 3 -Skutterudite: A Way Toward a Beneficial Composite Effect

Cédric Bourgès, Wenhao Zhang, Krushna Kumari Raut, Yuka Owada, Naoyuki Kawamoto, Masanori Mitome, Kazuaki Kobayashi, Jean-François Halet, David Berthebaud, Takao Mori

Investigation of Mn Single and Co-doping in Thermoelectric $CoSb_3$-Skutterudite: A Way Toward a Beneficial Composite Effect

Journal:	*ACS Applied Energy Materials*
Manuscript ID	ae-2023-017254.R2
Manuscript Type:	Article
Date Submitted by the Author:	n/a
Complete List of Authors:	BOURGÈS, Cédric; National Institute for Materials Science, Internation Center for Young Scientist (ICYS) Zhang, Wenhao; National Institute for Materials Science, WPI-MANA; University of Tsukuba Graduate School of Pure and Applied Sciences Raut, Krushna Kumari; National Institute for Materials Science, WPI-MANA; University of Tsukuba Graduate School of Pure and Applied Sciences Owada, Yuka; National Institute for Materials Science, Electron Microscopy Analysis Station/High-Resolution Group Kawamoto, Naoyuki; National Institute for Materials Science, Electron Microscopy Analysis Station/High-Resolution Group Mitome, Masanori; National Institute for Materials Science, Electron Microscopy Analysis Station/High-Resolution Group Kobayashi, Kazuaki; National Institute for Materials Science, WPI-MANA Halet, Jean-Francois; National Institute for Materials Science, CNRS-Saint Gobain-NIMS, IRL 3629, Laboratory for Innovative Key Materials and Structures (LINK) Berthebaud, David; National Institute for Materials Science, CNRS-Saint Gobain-NIMS, IRL 3629, Laboratory for Innovative Key Materials and Structures (LINK); Institut des Matériaux de Nantes Jean Rouxel, Nantes Université, CNRS Mori, Takao; National Institute for Materials Science, WPI-MANA; University of Tsukuba Graduate School of Pure and Applied Sciences

Investigation of Mn Single and Co-doping in Thermoelectric $CoSb_3$-Skutterudite: A Way Toward a Beneficial Composite Effect

Cédric Bourgès[1*], Wenhao Zhang[2,3], Krushna Kumari Raut[2,3], Yuka Owada[4], Naoyuki Kawamoto[4], Masanori Mitome[4], Kazuaki Kobayashi[2], Jean-François Halet[5], David Berthebaud[5,6], and Takao Mori[2,3*]

[1] *International Center for Young Scientists (ICYS), National Institute for Materials Science, Namiki 1-1, Tsukuba, Ibaraki 305-0044, Japan*

[2] *WPI-MANA, National Institute for Materials Science (NIMS), Namiki 1-1, Tsukuba, Ibaraki 305-0044, Japan*

[3] *Graduate School of Pure and Applied Sciences, University of Tsukuba, 1-1-1 Tennoudai, Tsukuba, Ibaraki 305-8577, Japan*

[4] *Electron Microscopy Analysis Station/High-Resolution Group, National Institute for Materials Science (NIMS), Namiki 1-1, Tsukuba, Ibaraki 305-0044 Japan*

[5] *CNRS-Saint Gobain-NIMS, IRL 3629, Laboratory for Innovative Key Materials and Structures (LINK), National Institute for Materials Science (NIMS), Namiki 1-1, Tsukuba, Ibaraki 305-0044, Japan*

[6] *Nantes Université, CNRS, Institut des Matériaux de Nantes Jean Rouxel, IMN, F-44000 Nantes, France*

Corresponding Authors: BOURGES.Cedric@nims.go.jp, MORI.Takao@nims.go.jp

Keywords*: Thermoelectric, $CoSb_3$, Manganese doping, Tellurium doping, Composites,*

ABSTRACT:

We report here the first in-depth theoretical and experimental investigations of Mn substitution within the $CoSb_3$-skutterudite. A systematic and comprehensive approach was employed to first determine the feasibility of single/co-substitution for Mn with Te and then assess its effect. Subsequently, experimental realization of the samples was conducted. We were able to highlight a low solubility limit of Mn as a single dopant and provide evidence that the substitution stabilizes *p*-type conduction as predicted *via* DFT calculations. Then, we reveal the prevalent formation of the composite MnTe/$CoSb_3$-skutterudite phases instead of the expected favorable co-substitution. This unexpected composite formation induces a beneficial effect, maximizing the Seebeck coefficient and leading to a record power factor $PF \approx 4.7$ mW/m.K^2 at 725 K for an unfilled skutterudite compound. ($PF = S^2\sigma$ with S, Seebeck coefficient; σ, electrical conductivity)

1 INTRODUCTION

Thermoelectric (TE) power generation represents a valuable solution for supplying a substantial amount of IoT applications and contributing to a sustainable future.[1,2] By utilizing appropriate devices, TE modules can effectively harvest waste heat from the surrounding environment and convert it into valuable electrical power. The TE conversion efficiency is quantified by the dimensionless figure of merit $zT = PFT\kappa^{-1} = S^2\sigma T\kappa^{-1}$ (*PF*, power factor; *T*, absolute temperature; *S*, Seebeck coefficient; σ, electrical conductivity; κ, thermal conductivity). In the range of ambient to mid-temperature (300 – 800 K), several compounds were reported with *zT* values above unity and beyond, such as Bi_2Te_3,[3,4] PbTe,[5,6] GeTe,[7,8] as well as the Mg_3Sb_2-based compounds[9,10] which have been extensively studied recently, leading to a theoretical conversion efficiency of 7 – 14%. However, most of those materials contain expensive and/or toxic elements which limit or even prevent their large applications. Other families of compounds, such as the oxide and sulfide compounds also appear to be attractive due to their low cost and/or eco-friendlier compositions but still show relatively modest *zT* values.[11] Among these families, there are ZnO,[12,13] some natural sulfide-based minerals such as the recent colusites $Cu_{26}T_2M_6S_{32}$ (T = V, Nb, Ta, Cr, Mo, W, Ti, M = Ge, Sn, Sb)[14,15] to mention a few.

In this context, the skutterudite $CoSb_3$ and derivatives represent an attractive solution for achieving the best trade-off between performance and scalability. Within the state-of-the-art thermoelectrics, $CoSb_3$ has been at the center of extensive investigations as a suitable compound where the concept of phonon-glass-electron crystal (PGEC) can apply for effectively decoupling its thermal and electrical transport properties and promoting a high figure of merit ($zT > 1$).[16] Indeed, it has been extensively studied during the past two decades and it is one of the few TE materials which step up to the stage of real applications such as for the next generation of RTG (Radioisotope Thermoelectric Generator) in the National Aeronautics and Space Administration (NASA) to replace the actual PbTe/GeTe-$AgSbTe_2$ (TAGS) couple, for instance.[17,18] Multiple intrinsic advantages of the skutterudites include strong mechanical strength,[19] reasonable thermal stability,[20] and both conductivity *p*- and *n*-types are achieved with high thermoelectric performances.

Additionally, the skutterudite-type structure is famous for its two icosahedral voids (2*a* site: (0;0;0)), present in its body-centered cubic structure (space group $Im\bar{3}$; $a \approx 9.04$ Å), which can be 'filled' by additional elements.[21,22] In general, the filler elements occupying the cavities in the structure are weakly bonded with their surrounding Sb atoms, allowing a rather efficient phonon scattering *via* rattling motion. Interestingly, this scattering does not significantly affect the electronic transport properties of the skutterudites, leading to impressive performances with *zT* values largely exceeding the unity in the

medium temperature range and even reaching a record value above 2 in the case of multi-filler-containing compounds assisted with strain defects.[23] However, the most efficient fillers are lanthanides, actinides, alkaline or alkaline-earth metals, raising some issues regarding the cost and availability of rare-earth elements, as well as the chemical stability and oxidation sensitivity of such filled-skutterudites.

In the present study, we focus on the investigation of inserting Mn element as a single and co-dopant within the $CoSb_3$-skutterudite structure. Prior studies presented a possibility of Mn insertion[24–26] in $CoSb_3$. The purpose of this study was to evaluate the effect of a strategic magnetic element on the thermoelectric properties of *n*-type skutterudites. Magnetism has been noted to effectively enhance the Seebeck coefficient in various recent examples such as via spin-carrier interaction,[27–31] spin fluctuation, or spin entropy.[32,33] The induced magnetic moment here can potentially influence the carriers through spin-carrier interactions affecting and enhancing the Seebeck coefficient.[29] Besides, co-doping is an attractive strategy that can be used to effectively enhance the solubility limit of substituted elements, defects, or impurities enabling the adjustment of the physicochemical, electronic, and magnetic properties of materials.[34] The well-known Te substitution was selected as co-dopant to i) stabilize the *n*-type conduction with high initial electronic transport properties, and ii) reduce the thermal conductivity of the unfilled skutterudite. [35–43] Theoretical investigations were conducted to assess the feasibility of single/co-doping and predict their influence on the electronic transport properties of $CoSb_3$. Then, an experimental investigation of the Mn-doped $CoSb_3$ and Mn-Te-codoped $CoSb_3$ was performed by solid-liquid state synthesis method followed by spark plasma sintering (SPS). A structural and microstructural analysis was systematically performed and discussed together with the characterization of the transport properties.

2 EXPERIMENTAL PROCEDURES

Sample Preparation. Samples of $Mn_xCo_{1-x}Sb_3$ (x = 0, 0.05, 0.10) and $Mn_xCo_{1-x}Sb_{2.85}Te_{0.15}$ (x = 0.005, 0.02, 0.04, 0.06, 0.08, 0.10) were prepared by melt-quenching processing. This was followed by extensive annealing in evacuated sealed tube processing and final consolidation by spark plasma sintering (SPS). Firstly, the stoichiometric ratio of high-purity shot elements (5 N) was weighted and sealed in carbon-coated evacuated quartz tubes. The tubes were heated up to 1423 K (heating rate of 100 K/h) and quenched in water. The resulting ingots were sealed in a new evacuated quartz tube and followed by an annealing at 873 K (heating rate of 100 K/h) for 100h to improve the homogeneity of the sample and facilitate the reaction of the residual free Sb. The annealed pellets were ground and sieved down to < 212 µm before being sintered (SPS-1080 – SPS Syntex Inc.) at 873 K for 5 min. (heating rate ~100 K/h) with an axial

pressure of ~50 MPa in a 10 mm diameter graphite die and partial vacuum atmosphere. The sintered pellets were then polished and cut to the required shapes and dimensions for the property measurements.

Characterizations. The crystal structure of different samples was investigated by X-ray diffraction (XRD) technique in the θ–2θ mode within a 10°–100° range (Smart Lab3 Rigaku Corporation apparatus). X-ray powder diffraction patterns were refined by Rietveld analysis using the FullProf and WinPLOTR software packages.[44,45] The shape of the diffraction peaks was modeled using a Thompson–Cox–Hastings pseudo-Voigt profile function. Zero-point shift, asymmetry parameters, and lattice parameters were systematically refined, and the background contribution was manually estimated.

Observations of fractured cross-sections of densified pellets by scanning electron microscopy (SEM) were performed using a Hitachi SU-8000 microscope and the chemical component analysis was carried out by energy dispersive spectroscopy (EDS) on polished surfaces.

The carrier concentration and mobility were obtained from Hall Effect measurements in AC transport by using a PPMS (Quantum design) from –5 to +5 T.

The electrical conductivity (σ) and Seebeck coefficient (S) were simultaneously measured by the four-probe method from 300 K up to 725 K using a ZEM-3 (ULVAC Advance-Riko) device under partial helium pressure. The estimated measurement uncertainties were fixed at 8% for the electrical conductivity and 6% for the Seebeck coefficient.[46]

The temperature-dependent thermal diffusivity (D) was measured using the laser flash diffusivity method with an LFA-467 Hyperflash (Netzsch) instrument on graphite-coated disc-shaped samples of 10 mm diameter and ~2 mm thickness. The temperature-dependent heat capacity (C_p) was derived using a standard sample (pyroceram-9060) with LFA-467, which was in good agreement with the expected Dulong–Petit C_p value. The total thermal conductivity was calculated using the formula, $\kappa = D \times C_p \times \rho$, where ρ is the density of the sample (measured using Archimedes' principle). In some cases, to better understand the thermal transport properties, the contributions from electronic and lattice parts in the total thermal conductivity were separated. The lattice thermal conductivity (κ_{latt}) was estimated from κ by subtracting the electronic contribution (κ_e) *via* the Wiedemann-Franz law, using the following equation,

$$\kappa_e = L\sigma T \quad (1)$$

where κ_e is the electronic thermal conductivity, and $L = 2.44 \times 10^{-8}$ V^2/K^2 is the Lorenz number. The uncertainty in the results was estimated to be 11% and 10% for the values of electrical and thermal

transport properties, respectively, and that for the overall zT was 15%.[46] Error bars are not shown in the figures in order to improve their readability.

Zero-field-cooled (ZFC), field-cooled-cooling (FCC), and field-cooled-warming (FCW) magnetization measurements were carried out on powder samples (~ 20 - 40 mg) from 2 to 300 K using a Magnetic Properties Measurement System (MPMS, Quantum Design) apparatus.

Theoretical Calculations. Density Functional Theory (DFT) calculations were carried out for the ground state of $CoSb_3$ and its doped derivatives. Self-consistent calculations were performed using a plane wave expansion basis set as implemented in the *Quantum Espresso* package[47] with the generalized gradient approximation pseudopotential (PBE-GGA) formulated with the projector augmented-wave (PAW) method.[48–50] A kinetic energy cutoff of 150 Ry and a 7 times higher charge density cutoff were used.

Defect formation energy calculations were performed to identify the defect sites of Mn/Te and their corresponding charge states. Mn and Te defects were relaxed at the Γ point of the Brillouin zone (BZ) while the total energy was calculated using a $4 \times 4 \times 4$ k-grid. Spin-nonpolarized calculations were used to obtain defect formation energies while collinear spin-polarized calculations were used for the band structure. In $CoSb_3$, defects can be positioned in one of the four different positions: 1) atomic substitution, 2) void-center, 3) 7-fold, and 4) 6-fold (the notation used is the same as that used in previous works).[51–53] In the latter three cases the extrinsic atoms form interstitial defects. The defect formation energy was given by the following equation,[54,55]

$$E_{def}(q) = E^{def}_{supercell}(q) - \sum_{\alpha} N_{\alpha}\,\mu_{\alpha} + q\mu_e + E_{corr}$$

where $E_{def}(q)$ is the defect formation energy of a charged defect, q refers to the charge state of the defect, $E^{def}_{supercell}(q)$ is the total energy of the charged defect-containing supercell, N is the number of atoms in the defect supercell and μ their corresponding chemical potential, μ_e is the chemical potential of the electron, and E_{corr} is the correction energy due to the mirror charges in the DFT calculations.[54–56] The chemical potentials of the atoms were determined under the equilibrium condition of phase coexistence. For Te doping, we calculated the chemical potential considering the phase equilibrium between $CoSb_3$, $CoSb_2$, and Sb_2Te_3. For Mn substitution, we chose the equilibrium $CoSb_3$, $CoSb_2$, and MnSb while for interstitial doping we chose the equilibrium between $CoSb_3$, Sb, and MnSb. Equaling the atomic chemical potential in the equilibrium phase gives the chemical potential used in the above equation.

3 RESULTS AND DISCUSSION

Effect of Mn Doping on Band Structure. Before carrying out any experiments, we decided to perform DFT calculations to study the effect of Mn doping and Mn/Te co-doping in $CoSb_3$. First, the defect positions of the Te and Mn dopants were determined from the calculated defect formation energy of different possible defect sites as a function of the electronic chemical potential and defect charge states, as shown in **Figure 1**. For both cases, substitution defects are energetically favored near the conduction band minimum (CBM) for Te doping and valence band maximum (VBM) for Mn doping. Indeed, the formation energy of the different dopant sites agrees systematically with that obtained in previous calculations.[51–53] In the *n*-type region, Te substitution has a defect charge state of +1 with respect to Sb, while the Mn substitution has a defect charge state of –2 with respect to Co.[56]

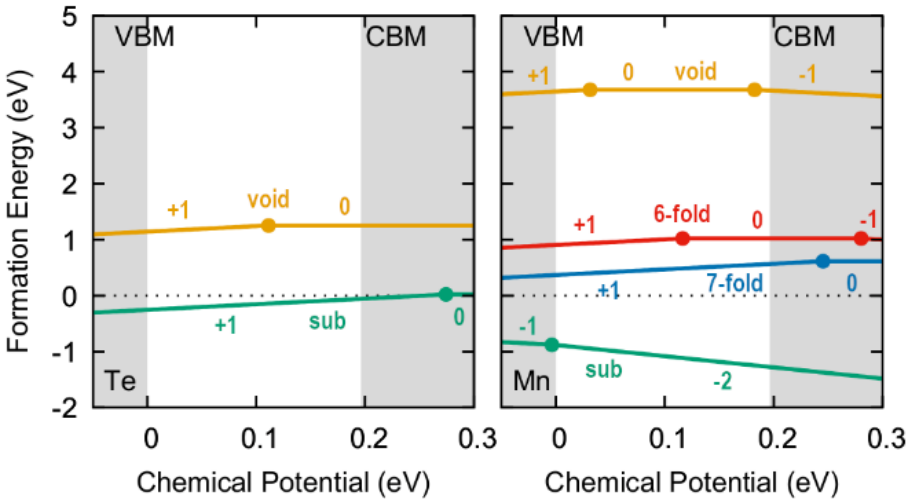

Figure 1 *Calculated defect formation energy for Te (left) and Mn (right) defects in $CoSb_3$. The green, orange, blue, and red colors refer to defects positioned at the four different possible positions, i.e., substitution, void-center, 7-fold, and 6-fold sites. The corresponding stoichiometries were $Co_{32}Sb_{95}Te$ (sub), $Co_{32}Sb_{96}Te$ (void), $MnCo_{31}Sb_{96}$ (sub), and $MnCo_{32}Sb_{96}$ (void, 6-fold and 7-fold).*

The effect of Mn substitution and co-doping on the electronic band structure of $CoSb_3$ is shown in **Figure 2**. The shape of the band structure and the band gap of 0.2 eV of the pure skutterudite $CoSb_3$ is in good agreement with previous theoretical calculations.[38,52,57,58] The top of the valence band around Γ consists mainly of Sb *p* states, showing an almost linear Kane band dispersion, while the bottom of the conduction band is mainly of Co 3*d* character. The introduction of Mn substitution leads to (flat and spin-polarized) impurity bands near the top of the valence band (**Figure 2b**) and a magnetic moment of 1.97 μ_B per substitutional defect, corresponding in turn to the difference in the number of valence electrons between Mn and Co. Except for the appearance of flat impurity bands around the Fermi level (orange

dotted line), the valence band dispersion remains essentially the same as that of pure $CoSb_3$, indicating that the effect of Mn substitution is localized.

For the co-doped systems, we considered that the main effect of co-doping with Te was to introduce additional electrons to the system (rigid band model approach). Therefore, **Figure 2c and d** shows the corresponding band structures of the Mn-substituted $CoSb_3$ with an additional number of electrons corresponding to co-doped systems. It turns out that these additional electrons fill the empty impurity bands deriving from Mn-inserted atoms reducing correspondingly their magnetic moments. When all the impurity bands are filled, the local magnetic moments on the defect sites vanish and the filled impurity bands sit just below the Fermi level. This indicates that by controlling the ratio between Mn and Te co-doping, some magnetism can be introduced in the $CoSb_3$ system, and precisely tuned. Indeed, this result provides the opportunity to investigate a potential correlation between magnetism and thermoelectric properties. Furthermore, a change in the band structures for both *p*-type and *n*-type transport properties is noticeable, suggesting a possible improvement of the thermoelectric properties of these systems.

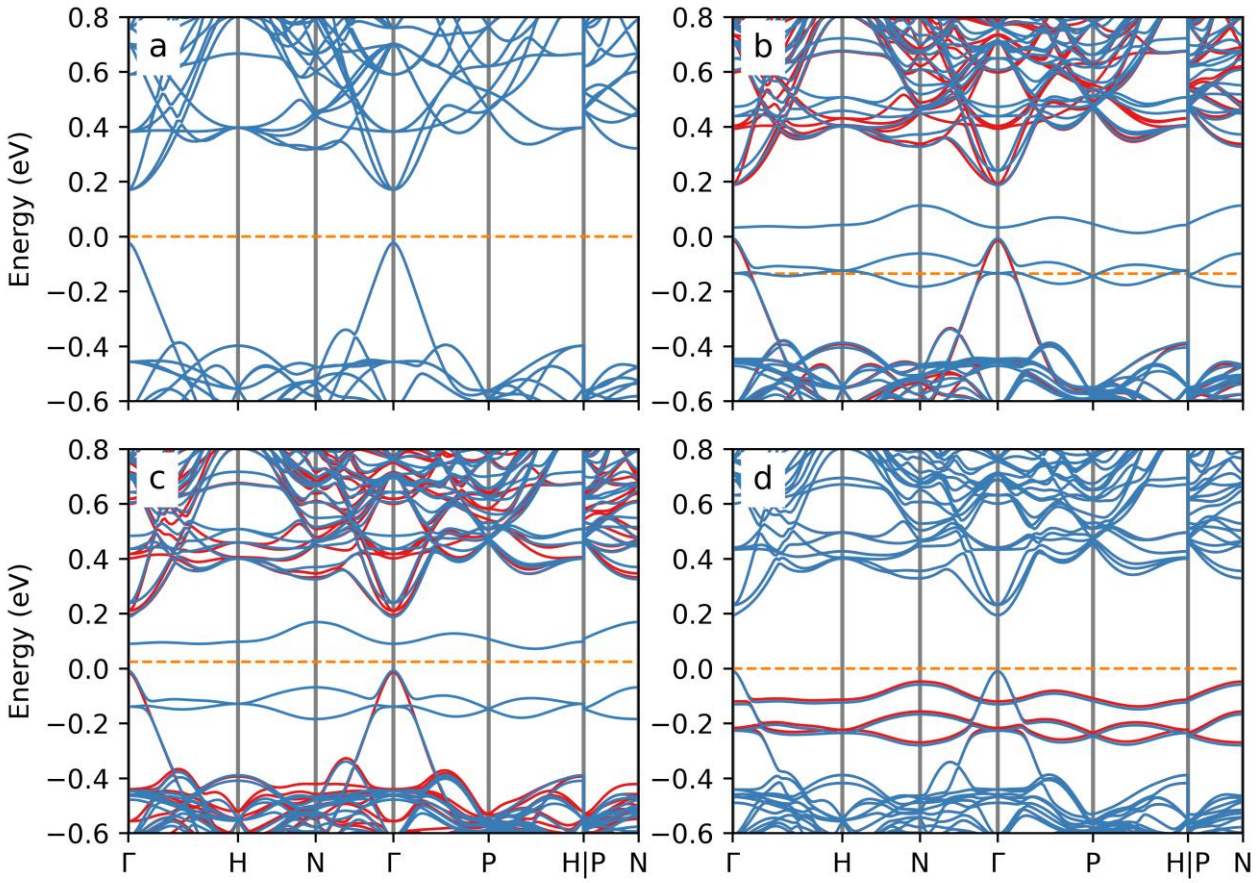

Figure 2 *Electronic band structure of a) $CoSb_3$, b) $Mn_{0.03}Co_{0.97}Sb_3$ ($MnCo_{31}Sb_{96}$ (sub)), c) $[Mn_{0.03}Co_{0.97}Sb_3]^-$ corresponding to formally $Mn_{0.03}Co_{0.97}Sb_{2.97}Te_{0.03}$, and d) $[Mn_{0.03}Co_{0.97}Sb_3]^{2-}$ corresponding formally to $Mn_{0.03}Co_{0.97}Sb_{2.94}Te_{0.06}$. Spin-up and spin-down bands are plotted in blue and red, respectively. The orange dotted line indicates the Fermi level.*

Mn Single-doped Influence in the TE Properties of $CoSb_3$. Figure 3 shows the X-ray powder diffraction (XRPD) patterns of the final Mn-doped samples densified by SPS. In all patterns, the main diffraction peaks corresponding to the $CoSb_3$-skutterudite structure ($Im\bar{3}$, $a \approx 9.04$ Å) can be observed with a trace amount of free Sb up to $x = 0.05$. Above this content, reflections barely observable at 2θ = 29.2º, 40.1º, and 43.4º agree with the formation of a tiny amount of the MnSb phase ($P\,6_3/m\,m\,c$, $a \approx$ 4.17 Å; $c \approx 5.76$ Å) which attests to an apparent solubility limit of the Mn within the $CoSb_3$ crystal structure. The formation of MnSb was confirmed through a Rietveld refinement analysis (**Figure S1**) as well as by SEM observations (**Figure S2**). The lattice parameter follows a pseudo linear trend up to x = 0.05 in relation with the Mn content increase within the $CoSb_3$ which is sustained by an EDX analysis (Table S1). However, beyond $x > 0.05$ the solubility limit is reached and the lattice parameter does not vary further as the favorable formation of MnSb occurs. The solubility limit is consistent with the valence electron count (VEC) deficiency in the Mn-doped $CoSb_3$ structure, as explained below. In the case of the prototypical MX_3 skutterudites (M = Co, Rh, and Ir) a VEC of 24 per formula is generally observed.[59] Assuming a successful tiny substitution of Co by Mn – thermodynamically stable according to the DFT calculations (see above) – the 2-electron poorer Mn element will reduce the theoretical VEC down to 23.8 for the $x = 0.1$ (see **Table 1**) explaining the *p*-type conduction observed even for a very small Mn amount. This result is similar to that of the Cr-doped $CoSb_3$ which highlighted a low solubility value of the 3*d* elements in the main structure.[60]

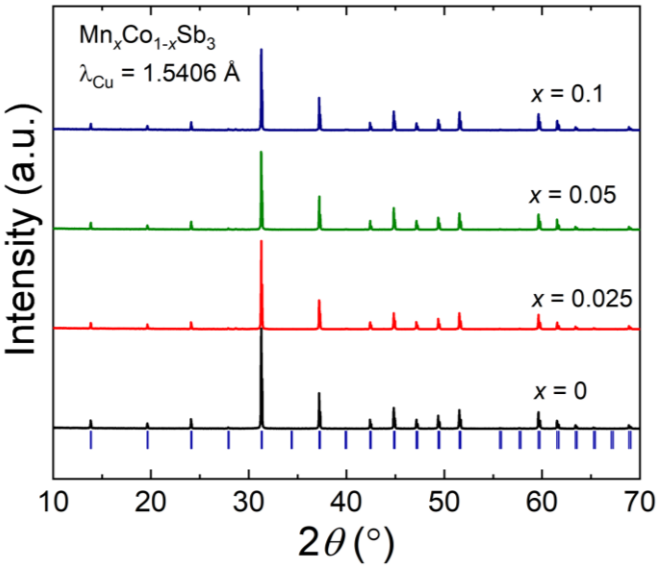

Figure 3 *X-ray powder diffraction pattern of the $Mn_xCo_{1-x}Sb_3$ SPS samples (x = 0, 0.025, 0.05, and 0.1).*

Table 1 *Rietveld refinement parameter of the X-ray powder diffraction patterns of the $Mn_xCo_{1-x}Sb_3$ SPS samples and theoretical valence electron count (VEC) per formula.*

$Mn_xCo_{1-x}Sb_3$, $I\,m\bar{3}$, λ_{Cu}						
x	*a* (Å)	*V* (Å^3)	χ^2	R_{Bragg}	R_F	VEC
0	9.0345	737.42	1.65	5.21	5.24	24
0.025	9.0337	737.21	1.74	6.28	6.48	23.95
0.05	9.0336	737.18	1.88	8.32	6.81	23.9
0.1	9.0336	737.19	1.98	8.96	8.05	23.8

x	B_{iso} (Co)	Co (occ.)	B_{iso} (Sb)	*y* (Sb)	*z* (Sb)	Sb (occ.)
0	0.5	1	0.5	0.33438	0.15823	1
0.025	0.5	1	0.5	0.33395	0.15798	1
0.05	0.5	1	0.5	0.33406	0.15797	1
0.1	0.5	1	0.5	0.33367	0.15712	1

The Seebeck coefficient *S* and the electrical resistivity ρ of the Mn-doped $CoSb_3$ samples over the temperature are sketched and compared to a pristine $CoSb_3$ reference sample in **Figure 4**. It is noteworthy to remind that in pure $CoSb_3$ the carrier type obtained at room temperature depends on whether the samples are synthesized under Sb-rich or Sb-deficient conditions. Samples grown under Sb-rich conditions will be *p*-type since this corresponds to the formation of holes in the valence band promoted by the absence of some Co atoms. On the contrary, samples synthesized with Sb-deficient conditions will lead to an excess of electrons in the conduction band and consequently *n*-type behavior. No excess Sb was used in our synthesis, but our reference sample shows *n*-type conduction at room temperature which turns to *p*-type conduction above 330 K as expected from a slightly Sb deficient sample. Indeed, Mn doping changes the *n*-type character into a stable *p*-type conduction all over the temperature range (**Figure 4a**). This constitutes the first report illustrating that Mn substitution can modify the thermoelectric properties in skutterudites. The Seebeck coefficient |*S*| increases gradually from $x = 0.025$ to 0.05 in the single-phase region before decreasing together with the formation of MnSb for $x = 0.1$ implying that the secondary phase affects the electrical transport properties. This increase in the Mn-doped sample is attributed to the formation of the flat impurity bands near the top of the valence band, which enhances the density of states around the Fermi level (see **Figure 2b** above). Indeed, this increase of DOS must play a significant role in the enhancement of the Seebeck coefficient which according to the Mott's formula for a metal/degenerate-semiconductor can be defined as:[61]

$$S = \frac{\pi^2}{3}\frac{k_B^2 T}{e}\left(\frac{d\{ln[\sigma(E)]\}}{dE}\right)_{E=E_F}$$

with k_B, the Boltzmann's constant and *e* the electron elementary charge. The large magnitude of the Seebeck coefficient at room temperature is also consistent with a low carrier concentration in the range of $10^{16} – 10^{17}$ cm^{-3} as confirmed by Hall effect measurements. The *S* and σ *vs.* the hole concentration *p* plots (**Figure 5a**) reveal a parabolic and linear trend confirming the carrier concentration's dependence on the electrical transport properties despite the apparent lack of trend with the nominal Mn-content. Irrespective of the Mn content, the electronic transport properties in the near room temperature range (300 – 450 K) are significantly enhanced with an averaged three-time improvement ($PF_{\text{av300–450 K}}$) (**Figure 4c**). This improvement can certainly be attributed to the large *p*-type Seebeck coefficient and the reduced electrical resistivity. However, in the higher temperature range (T > 450 K) PF_{max} of the undoped sample remains the highest one due to a slightly larger electrical conductivity. It is likely related to the increased carrier scattering at higher temperatures due to the impurity phases (Sb and Sb/MnSb) occurring only in Mn-doped samples. Indeed, those trends follow well the calculated weighted mobilities showing larger values in the low temperature for the Mn-doped samples which converge in the high temperature ranges T > 450 K to similar values (**Figure 5b**). The weighted mobility can be defined as:[62]

$$\mu_W = \frac{3h^3}{8\pi e\rho(2m_e k_B T)^{3/2}}\left[\frac{exp\left[\left(\frac{|S|}{k_B/e}\right)-2\right]}{1+exp\left[-5\left(\frac{|S|}{k_B/e}\right)-1\right]}+\frac{\frac{3}{\pi^2}\frac{|S|}{k_B/e}}{1+exp\left[5\left(\frac{|S|}{k_B/e}\right)-1\right]}\right]$$

with μ_W the weighted mobility, ρ the electrical resistivity, *T* the absolute temperature, *S* the Seebeck coefficient, and $\frac{k_B}{e} = 83.3\ \mu V/K$. The large weighted mobilities show an increasing dependence in temperature for samples with $x > 0$, suggesting that the defects (Mn ionized dopants) are responsible for the superior *PF*. However, at the temperature $T > 450$ K, the decreasing dependence confirms that the usual phonon scattering mechanism is at work for the electrical transport properties and limits the role of the impurities.

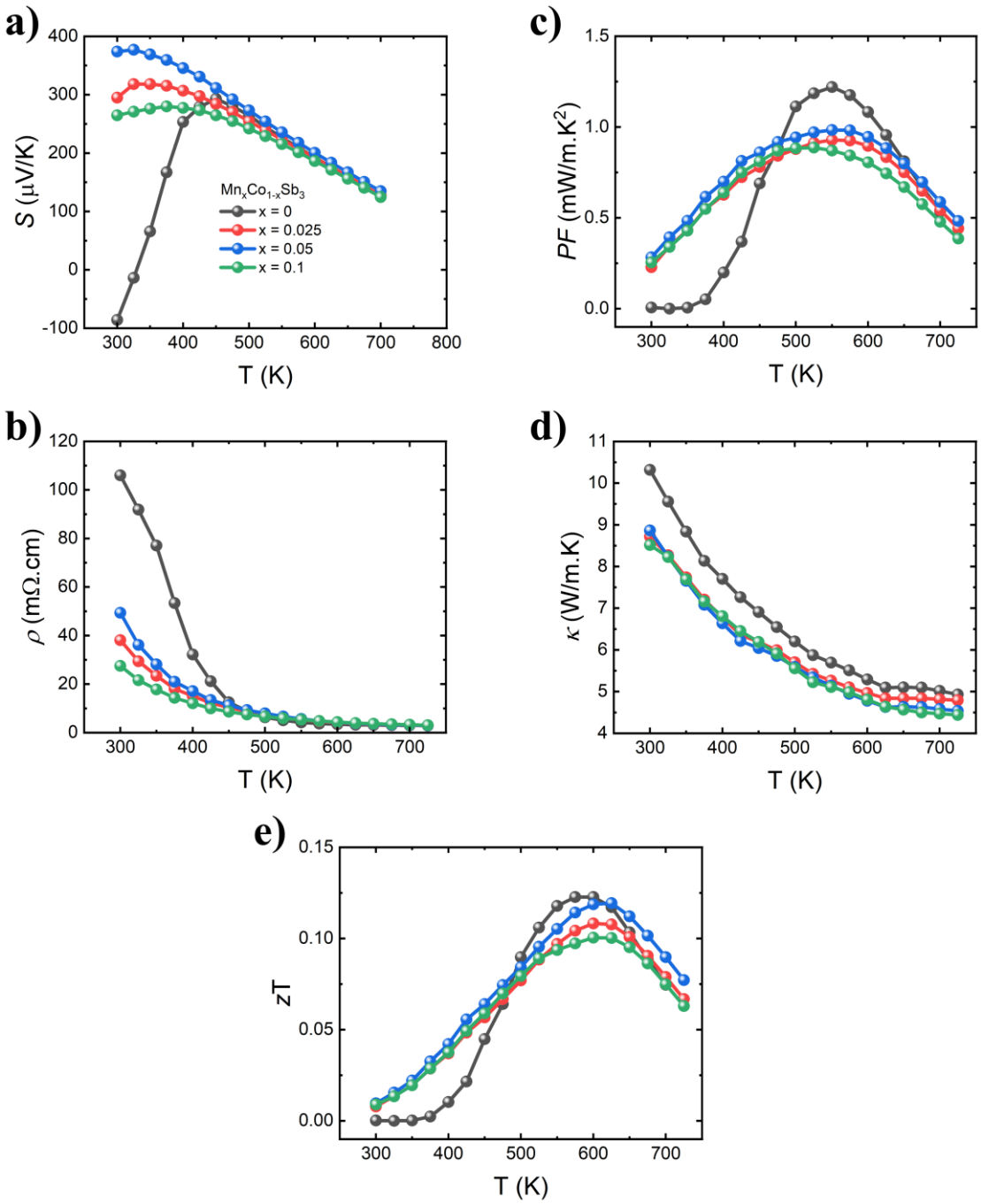

Figure 4 *a) Seebeck coefficient S, b) electrical resistivity σ, c) power factor PF, d) thermal conductivity κ, and e) figure of merit zT as function of temperature of $Mn_xCo_{1-x}Sb_3$ SPS samples. The estimated measurement uncertainties are 6% for the S, 8% for ρ, 11% for the PF, 10%, for the κ and 15% for the zT.* [46]

The thermal conductivity of the Mn-doped samples diminishes slightly with respect to that of pure $CoSb_3$ throughout the entire temperature range (**Figure 4d**). This diminution is in an agreement with the slight mass fluctuation scattering of the phonons induced by the substitution of Co (58.933 g/mol) by Mn (54.938 g/mol). It is not excluded that the presence of MnSb impurity within the matrix for $x = 0.1$ might

contribute to this decrease but its role is considered as minor due to the small amount in presence. Anyway, the thermal conductivity remains still too large for promoting a better figure of merit and the *zT* values follow in turn the trend of the *PF* variations (**Figure 4e**).

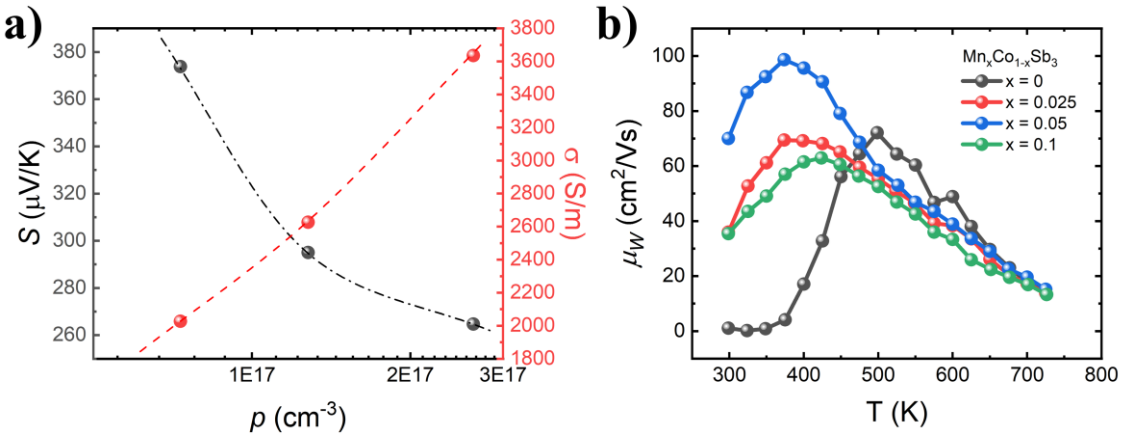

Figure 5 *a) S and σ dependence upon hole concentration p at 300 K, and b) weighted mobility dependence in temperature of $Mn_xCo_{1-x}Sb_3$ SPS samples.*

Mn Co-doped Influence in the TE Properties of *n*-type $CoSb_3$. We further used Te co-doping to investigate the *n*-type transport region of the $CoSb_3$ skutterudite with Mn impurities. The approach was to over-dope with Te to compensate the Mn doping effect demonstrated above. Indeed, the Te-single doping on the $CoSb_3$ matrix has been extensively explored theoretically and experimentally within the past two decades.[35–43] The role of Te as an electron donor as well as a phonon scattering center due to the mass fluctuation effect have been demonstrated and used for promoting large figures of merit in unfilled $CoSb_3$-skutterudites. From the electronic band-structure point of view, although Te doping only slightly influences the shape of the top of the valence band, it somewhat shifts the Fermi energy level up to the conduction band and reduces the width of the bottom of the conduction band. This variation of the band gap and conduction band width implies some increase in both carrier concentration and effective mass for an overall enhanced electrical performance. Experimentally, Te-doping in $CoSb_{3-y}Te_y$ was investigated in the formula range $0 \leq y \leq 0.20$, the latter constituting the solubility limit of Te content within the bulk $CoSb_3$ structure. Classically, the optimum figure of merit *zT* is obtained with the content $y \approx 0.125$ due to the trade-off between the reduction of the thermal conductivity and the maintaining of a large *PF* independently of the process employed.[37,40,43] To achieve higher *zT* and compensate the theoretical electron deficiency induced by Mn substitution, the Te content for the co-doping was fixed at a slightly over doping $y = 0.15$.

Figure 6 shows the X-ray powder diffraction (XRPD) patterns of the final $Mn_xCo_{1-x}Sb_{2.85}Te_{0.15}$ densified samples. In all patterns, the main diffraction peaks corresponding to the $CoSb_3$-skutterudite structure ($Im\bar{3}$, $a \approx 9.04$ Å) can be observed. In the case of the Mn-based doped samples ($x > 0$), Mn

doping promotes the formation of the MnTe phase ($P\,6_3/m\,m\,c$, $a \approx 4.14$ Å; $c \approx 6.70$ Å)[63] confirmed through an EPMA mapping analysis (**Figure 7**) and its corresponding point analysis (**Figures S3-S4**).

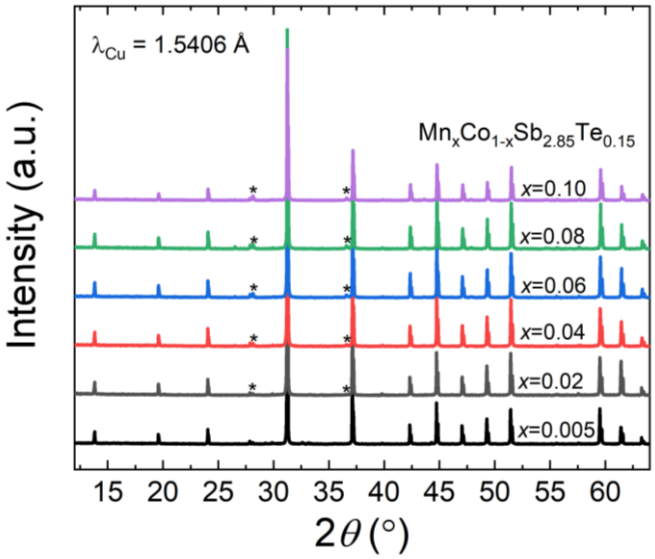

Figure 6 *X-ray powder diffraction patterns of the $Mn_xCo_{1-x}Sb_{2.85}Te_{0.15}$ SPS samples after annealing.*

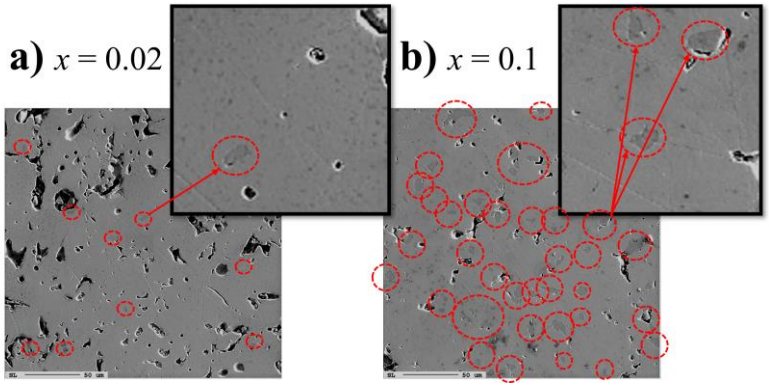

Figure 7 *EPMA images of the $Mn_xCo_{1-x}Sb_{2.85}Te_{0.15}$ SPS samples (x = 0.02 (a) and 0.1 (b)) after annealing. The red circles indicate the MnTe inclusions within the $CoSb_3$ matrix.*

Contrary to the Mn single-doped samples, Mn substitution in the Co site appeared not to be favorable in presence of Te and led to the unavoidable precipitation of nano-microscale size MnTe particles. The distribution of the MnTe inclusions is homogeneous with a varying size distribution ranging from the nanometer scale to few microns, characterized by an angular medium sphericity roundness. A Rietveld refinement allowed us to estimate the wt.% of MnTe in each sample. The results are shown in **Table 2**. The MnTe-phase content increases with *x* content from 1.15 wt.% for *x* = 0.02 to 4.76 wt.% for *x* = 0.1, as illustrated with the EPMA images shown in the **Figure 7**.

Table 2 *Rietveld refinement parameters of the X-ray powder diffraction patterns of the $Mn_xCo_{1-x}Sb_{2.85}Te_{0.15}$ SPS samples and estimation of the mass fraction percentage (wt.%) of each phase ($CoSb_3$ and MnTe)*

$Mn_xCo_{1-x}Sb_{2.85}Te_{0.15}$, $Im\bar{3}$, λ_{Cu}							
x	*a* (Å)	*V* (Å^3)	χ^2	R_{Bragg}	R_F	*wt.*% ($CoSb_3$)	*wt.*% (MnTe)
0.005	9.050(1)	741.1	2.27	9.99	6.7	100	-
0.02	9.049(1)	741.0	2.61	8.86	7.6	98.9	1.1
0.04	9.046(1)	740.1	2.61	8.26	6.44	98.1	1.9
0.06	9.043(1)	739.4	2.65	8.81	7.62	96.8	3.2
0.08	9.040(1)	738.9	2.91	10.2	7.34	96.0	4.0
0.1	9.039(1)	738.7	2.79	12.7	10.3	95.8	4.2

x	B_{iso} (Co)	Co (occ.)	B_{iso} (Sb/Te)	*y* (Sb/Te)	*z* (Sb/Te)	Sb (occ.)	Te (occ.)
0.005	0.292	1	0.246	0.3339	0.1581	0.95	0.05
0.02	0.292	1	0.246	0.3337	0.1583	0.95	0.05
0.04	0.292	1	0.246	0.3341	0.1580	0.95	0.05
0.06	0.292	1	0.246	0.3342	0.1578	0.95	0.05
0.08	0.292	1	0.246	0.3336	0.1580	0.95	0.05
0.1	0.292	1	0.246	0.3339	0.1576	0.95	0.05

High accuracy of the EPMA point analysis revealed only some trace of Mn in the main $CoSb_3$ matrix confirming that the presence of Te prevents the substitution of the Co site due to the low enthalpy of formation of MnTe, reported to be $\Delta H_{298}^{s} = -40.2\ kJ.g.at^{-1}$.[64] In order to confirm the presence/absence of Mn within the Te-doped $CoSb_3$ structure, a STEM investigation was performed in two characteristic zone axes (namely [110] and [001]), (see **Figure 8a** and **8b**, respectively) in order to observe accurately the icosahedral voids (2*a* site: (0; 0; 0)) together with the global structural arrangement. As a result, the icosahedral voids appeared free of any filler and no intensity defects are observable in the HAADF image (**Figure 8a**). A TEM-EDS mapping (**Figure 8b**) confirmed that the Te substitution occurs at the Sb site but could not confirm the presence of Mn within the structure. To the best of our knowledge, the community has always been divided regarding the possibility or not that the tellurium element fills the skutterudite voids rather than substitutes the Sb site. It is noteworthy to point out here that the current STEM-HAADF we performed constitutes the first evidence that Te does not fill the icosahedral void of the skutterudite structure. Indeed, from a chemical point of view, it is hard to believe that Te anions can fill anionic Sb voids.

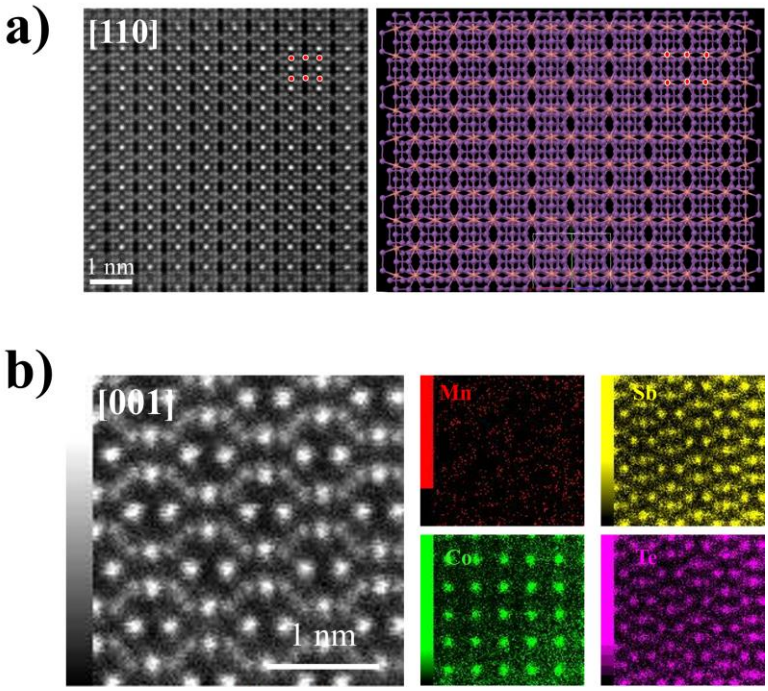

Figure 8 *STEM-HAADF images of a) the [110] axis and the corresponding structural model, and b) the [001] axis and the corresponding EDS mapping of the* $Mn_{0.1}Co_{0.99}Sb_{2.85}Te_{0.15}$ *SPS sample.*

The TE properties of the Mn/Te-co-doped $CoSb_3$ samples are illustrated in **Figure 9**. All samples exhibit a *n*-type conduction consistently with the Te-doping effect as reported in several previous studies (**Figure 9a**) and expected due to the Te electron donor properties. [35–43] Interestingly, the Mn *x* content induces a large increase of the absolute values of the Seebeck coefficient $|S|$ in the whole temperature range. Despite the concurrently rise of the electrical resistivity (**Figure 9b**), *PF* increases massively in the room temperature range from 2.29 to 3.56 mW/m.K^2 at 300 K for x = 0.005 and 0.1, respectively. This kind of large increase is usually not observed for unfilled $CoSb_3$ skutterudites. Interestingly, such a large enhancement of the electrical transport properties of the Mn-containing samples at room temperature is supported by the calculated weighted mobilities (**Figure 10b**) (see the Mn single doped section above). It can be observed that the weighted mobilities are overall large and decrease with temperature, a characteristic of most of the good thermoelectric materials, confirming that the electron-phonon scattering mechanism is dominant.[62] We can notice that the weighted mobilities range in the values μ_w > 300 cm^2/V at 300 K and reach the impressive value of 397 cm^2/V at 300 K for x = 0.1, comparable indeed to that reported for PbTe.[65]

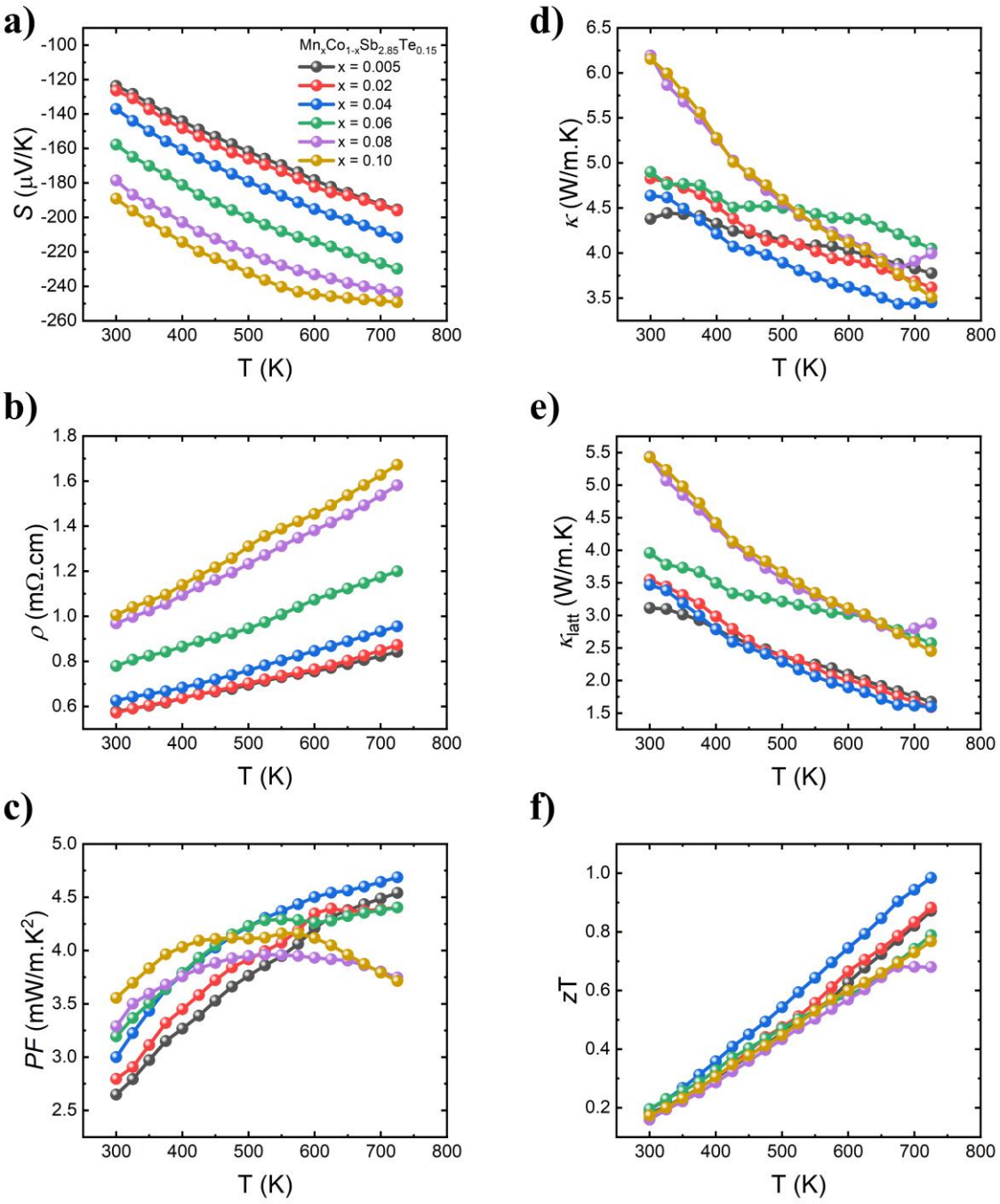

Figure 9 *a) Seebeck coefficient S, b) electrical resistivity σ, c) power factor PF, d) total thermal conductivity κ, e) lattice part of the thermal conductivity κ_{latt}, and f) figure of merit zT as function of temperature of the $Mn_xCo_{1-x}Sb_{2.85}Te_{0.15}$ SPS samples. The estimated measurement uncertainties are 6% for the S, 8% for ρ, 11% for the PF, 10%, for the κ and 15% for the zT.* [46]

The initial contribution to the increase of the Seebeck coefficient can be attributed to the decrease of the carrier concentration *n* resulting from a higher (total) Mn content, as demonstrated in **Figure 9**. Upon formation of the MnTe phase, the electron donor effect caused by the Te content in $CoSb_3$ is reduced (Figures S4-S5) since Te preferentially reacts with Mn. Consequently, the electron concentration

decreases, as indicated by the Hall effect measurements, from $n = 4.05 \times 10^{20}$ to 1.20×10^{20} cm^{-3} at 300 K, respectively, for $x = 0.02$, and 0.1 (**Figure 10a**). However, the slight carrier concentration variation cannot explain solely the major increase of the Seebeck coefficient, as evidenced by comparing the $Mn_xCo_{1-x}Sb_{2.85}Te_{0.15}$ samples with the single Te-doped series with the ratio 0.15–*x* (**Figure S5**). Indeed, the presence of the MnTe phase introduces a composite effect that may bring two additional contributions: i) the larger band gap of MnTe ($E_g \approx 0.6 – 1.2$ eV) compared to that of $CoSb_3$ ($E_g \approx 0.2$ eV) could be favorable to an energy filtering effect in the case of an energy level alignment between the electronic structures of $CoSb_3$ and MnTe around the Fermi level,[66,67] and/or ii) the (known) antiferromagnetic state of the MnTe phase can bring some local magnetic moments which can *couple* with the carriers of doped-$CoSb_3$ at the interface between the $CoSb_3$ matrix and the MnTe precipitate.[68,69] In both cases, the carriers should acquire a heavier effective mass leading to a superior Seebeck coefficient. To elucidate point ii), the magnetic behavior of the series ($x > 0.005$) was probed to get an insight regarding the Mn doping (**Figure S6**). All the susceptibilities were normalized with respect to the $CoSb_3$ molar mass rather that of the Mn content to conduct a comparative analysis. The apparent magnetic susceptibility increases with the Mn content in the near-room temperature range sustaining a possible role of magnetism in the observed properties upon co-doping. However, the presence of the antiferromagnetic (AFM) MnTe phase within the matrix (Tc = 308 K, $\mu_{eff} \approx 5$ μ_B per unit cell, $\theta \approx –600$ K) renders the determination of the residual magnetic moment within $CoSb_3$ somewhat hazardous.[63,70]

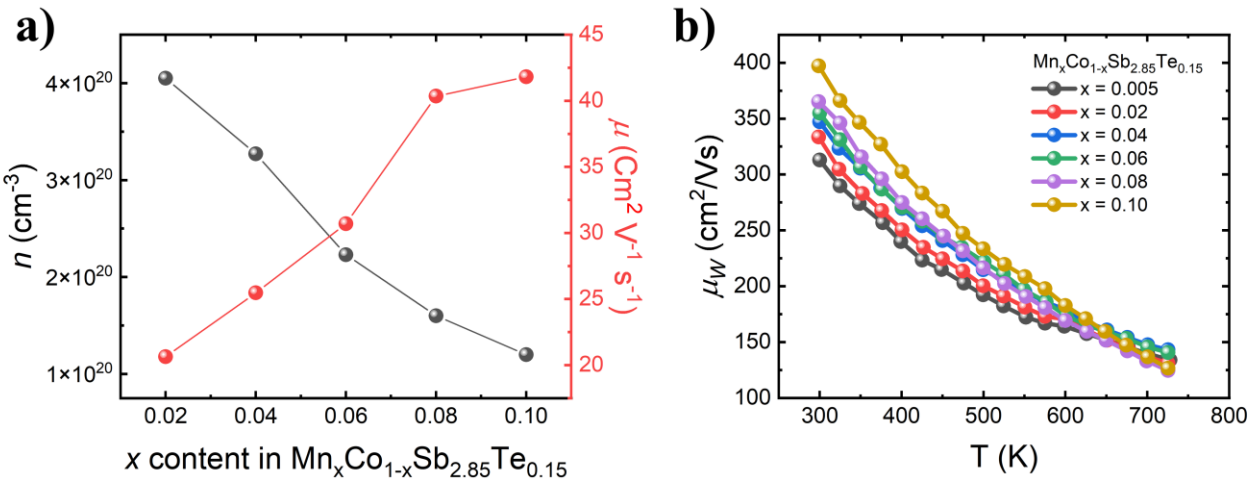

Figure 10 *a) Carrier concentration n and mobility μ at 300 K, and b) weighted mobility dependence in temperature of the $Mn_xCo_{1-x}Sb_{2.85}Te_{0.15}$ SPS samples*

Together with *PF*, the thermal conductivity κ increased with the increasing Mn content (**Figure 9d**). This increase is in large part attributed to the lattice contribution κ_{latt} (**Figure 9e**), attesting a change

in the phonon transport mechanism. This reveals that thermal transport is sensitive to the MnTe formation. Two set of samples can be separated: *i*) from x = 0.005 to 0.04, and *ii*) from x = 0.06 to 0.1. For *i*), the formation of MnTe is estimated to be below 2 wt.% (**Table 2**) and therefore the amount of the MnTe dispersion in $CoSb_3$ remains small, as illustrated in the EPMA image for x = 0.02 (**Figure 7a**). Interestingly, κ_{latt} remains at its lowest values despite the expected reduction in Te content within the $CoSb_3$ matrix. This indicates a proficient effect of the precipitate to act as a scattering center, enabling a slight reduction of κ (**Figure 9d**). At higher Mn content, κ increases gradually near room temperature, approaching a value close to that of the undoped $CoSb_3$. This increase is directly related to a massive rise of κ_{latt} of more than 50% in the whole temperature range for the samples x = 0.08–0.1. This is consistent with the large formation of MnTe, which reduces the Te content within the co-doped $CoSb_3$ structure and subdues its effect on the reduction of the thermal transport. As a result, the figure of merit is improved for x = 0.04 to maximum values of $zT \approx 1$ at 725 K thanks to a slight reduction of κ and a significant enhancement of *PF*. It is noteworthy that this ultra-high value of PF = 4.7 mW/m.K^2 at 725 K has been rarely obtained for rare-earth free skutterudites.

4 CONCLUSIONS

In summary, we have reported here the first theoretical and experimental investigation of the Mn doping effect on $CoSb_3$-skutterudite. An original approach was adopted focusing first on single Mn-doped $Mn_xCo_{1-x}Sb_3$ samples before exploring co-doping with Te to prepare $Mn_xCo_{1-x}Sb_{2.85}Te_{0.15}$ samples, examining their effect on both conduction types. Theoretical DFT results revealed that single Mn doping was feasible. This was successfully confirmed experimentally with the obtention of pure samples with a low solubility of Mn ($x \leq 0.05$ in $Mn_xCo_{1-x}Sb_3$) sitting at the Co site up to a certain amount of Mn substitution where a small amount of the binary MnSb phase is formed. Regarding the transport properties, we show for the first time that Mn stabilizes *p*-type conduction with a large Seebeck coefficient resulting from a small reduction of the valence electron count per formula due to some Co substitution. This allows an improvement of the power factor as well as the resulting figure of merit zT in the near-room temperature range (T < 450 K). Co-doping with Te was then realized highlighting that the formation of the additional MnTe phase was unexpectedly prevalent with respect to Co substitution. The structural investigation evidenced for the first time that Te is substituting Sb and does not fill the icosahedral voids present in the $CoSb_3$ skutterudite. We also revealed that a significant enhancement of the power factor can be achieved with ultra-high value of 4.7 mW/m.K at 725 K seldomly reported for rare-earth free skutterudites due to a spectacular increasing of the Seebeck coefficient in the co-doped $CoSb_3$ skutterudite. Combined experimental and theoretical findings indicate that a plethora of factors beneficially participate to the large

enhancement of the Seebeck coefficient, successfully allowing to achieve a maximum zT value of 1 at 725 K. Such a high value can in turn be controlled by the formation of some MnTe secondary phase which slightly helps to reduce the thermal conductivity and to maximize an unexpected power factor to a value which competes with that reported for the expensive rare-earth filled skutterudites. This achievement contributes to build up a divergent approach to the developpement of a new generation of sustainable TE materials by investigating the magnetic as well as the composite effect in order to provide stable, cost efficient and high performance materials for thermoelectricity based on unfilled skutterudites.

ASSOCIATED CONTENT

SI- Supporting Information

The Supporting Information is available free of charge at https://pubs.acs.org/doi/XXX

Refined powder X-ray diffraction pattern of the sample $Mn_xCo_{1-x}Sb_3$ for Mn = 0.1 after SPS. SEM image and EDS mapping of the polished sample $Mn_xCo_{1-x}Sb_3$ for Mn = 0.1 after SPS. Extended point analysis by EPMA of the $Mn_xCo_{1-x}Sb_{2.85}Te_{0.15}$ SPS samples (x = 0.02 and 0.1). Seebeck coefficient S, as function of temperature of the $Mn_xCo_{1-x}Sb_{2.85}Te_{0.15}$ and corresponding compensated Te-single doped $CoSb_{3-y}Te_y$ SPSed samples. Temperature-dependent magnetic susceptibility χ and $1/\chi$ of the $Mn_xCo_{1-x}Sb_{2.85}Te_{0.15}$ SPSed. Energy Dispersive X-ray analysis of $Mn_xCo_{1-x}Sb_3$.(PDF)

AUTHOR INFORMATION

Corresponding Authors.

Cédric Bourgès - International Center for Young Scientists (ICYS), National Institute for Materials Science, 1-1 Namiki, Tsukuba, Ibaraki 305-0044, Japan; orcid.org/0000-0001-9056-0420, Email: BOURGES.Cedric@nims.go.jp,

Takao Mori - WPI-MANA, National Institute for Materials Science (NIMS), Namiki 1-1, Tsukuba 305-0044, Japan and Graduate School of Pure and Applied Sciences, University of Tsukuba, 1-1-1 Tennoudai, Tsukuba, Ibaraki 305-8577, Japan; orcid.org/0000-0003-2682-1846, Email: MORI.Takao@nims.go.jp,

Authors.

Wenhao Zhang - WPI-MANA, National Institute for Materials Science (NIMS), Namiki 1-1, Tsukuba 305-0044, Japan and Graduate School of Pure and Applied Sciences, University of Tsukuba, 1-1-1 Tennoudai, Tsukuba, Ibaraki 305-8577, Japan, orcid.org/0000-0003-3359-1882

Krushna Kumari Raut - WPI-MANA, National Institute for Materials Science (NIMS), Namiki 1-1, Tsukuba 305-0044, Japan and Graduate School of Pure and Applied Sciences, University of Tsukuba, 1-1-1 Tennoudai, Tsukuba, Ibaraki 305-8577, Japan, orcid.org/0009-0009-7945-2838

Yuka Owada - Electron Microscopy Analysis Station/High-Resolution Group, National Institute for Materials Science (NIMS), Namiki 1-1, Tsukuba, Ibaraki 305-0044, Japan

Naoyuki Kawamoto - Electron Microscopy Analysis Station/High-Resolution Group, National Institute for Materials Science (NIMS), Namiki 1-1, Tsukuba, Ibaraki 305-0044, Japan, orcid.org/0000-0002-2022-3987

Masanori Mitome - Electron Microscopy Analysis Station/High-Resolution Group, National Institute for Materials Science (NIMS), Namiki 1-1, Tsukuba, Ibaraki 305-0044, Japan, orcid.org/0000-0003-1192-9838

Kazuaki Kobayashi - WPI-MANA, National Institute for Materials Science (NIMS), Namiki 1-1, Tsukuba 305-0044, Japan, orcid.org/0000-0002-3440-5730

Jean-François Halet - CNRS-Saint Gobain-NIMS, IRL 3629, Laboratory for Innovative Key Materials and Structures (LINK), National Institute for Materials Science (NIMS), Namiki 1-1, Tsukuba, Ibaraki 305-0044, Japan, orcid.org/0000-0002-2315-4200

David Berthebaud - CNRS-Saint Gobain-NIMS, IRL 3629, Laboratory for Innovative Key Materials and Structures (LINK), National Institute for Materials Science (NIMS), Namiki 1-1, Tsukuba, Ibaraki 305-0044, Japan and Nantes Université, CNRS, Institut des Matériaux de Nantes Jean Rouxel, IMN, F-44000 Nantes, France, orcid.org/0000-0002-2892-2125

Author Contributions.

Conceptualization, Methodology, Validation- CB; *Formal Analysis*- CB, WZ, YO & NK; *Investigation*- CB, WZ & KKR; *Writing-Original Draft*- CB; *Writing- Review & Editing*- CB, WZ, DB, JFH; *Resources, Funding acquisition*- TM; *Supervision*- TM, MM & KK

Notes.

The authors declare no conflict of interest.

ACKNOWLEDGMENTS.

This work was supported by JST Mirai Program JPMJMI19A1 and ICYS fellowship. The authors would like to acknowledge the Namiki Foundry (NIMS, Japan), SEM analysis and Material Analysis Station (NIMS, Japan) for EPMA and XRD analyses. The DFT calculations were performed using the numerical materials simulator [HPE SGI 8600] in NIMS, Japan.

REFERENCES

(1) Haras, M.; Skotnicki, T. Thermoelectricity for IoT – A Review. *Nano Energy* **2018**, *54*, 461–476. https://doi.org/10.1016/j.nanoen.2018.10.013.

(2) Petsagkourakis, I.; Tybrandt, K.; Crispin, X.; Ohkubo, I.; Satoh, N.; Mori, T. Thermoelectric Materials and Applications for Energy Harvesting Power Generation. *Sci. Technol. Adv. Mater.* **2018**, *19*, 836–862. https://doi.org/10.1080/14686996.2018.1530938.

(3) Witting, I. T.; Chasapis, T. C.; Ricci, F.; Peters, M.; Heinz, N. A.; Hautier, G.; Snyder, G. J. The Thermoelectric Properties of Bismuth Telluride. *Adv. Electron. Mater.* **2019**, *5*, 1800904. https://doi.org/10.1002/aelm.201800904.

(4) Zheng, Z.-H.; Shi, X.-L.; Ao, D.-W.; Liu, W.-D.; Li, M.; Kou, L.-Z.; Chen, Y.-X.; Li, F.; Wei, M.; Liang, G.-X.; Fan, P.; Lu, G. Q.; Chen, Z.-G. Harvesting Waste Heat with Flexible Bi_2Te_3 Thermoelectric Thin Film. *Nat. Sustain.* **2022**, *6*, 180–191. https://doi.org/10.1038/s41893-022-01003-6.

(5) Wu, Y.; Nan, P.; Chen, Z.; Zeng, Z.; Liu, R.; Dong, H.; Xie, L.; Xiao, Y.; Chen, Z.; Gu, H.; Li, W.; Chen, Y.; Ge, B.; Pei, Y. Thermoelectric Enhancements in PbTe Alloys Due to Dislocation-Induced Strains and Converged Bands. *Adv. Sci.* **2020**, *7*, 1902628. https://doi.org/10.1002/advs.201902628.

(6) Jang, H.; Park, J. H.; Lee, H. S.; Ryu, B.; Park, S. D.; Ju, H. A.; Yang, S. H.; Kim, Y. M.; Nam, W. H.; Wang, H.; Male, J.; Snyder, G. J.; Kim, M.; Jung, Y. S.; Oh, M. W. Regulating Te Vacancies through Dopant Balancing via Excess Ag Enables Rebounding Power Factor and High Thermoelectric Performance in *p*-Type PbTe. *Adv. Sci.* **2021**, *8*, 2100895. https://doi.org/10.1002/advs.202100895.

(7) Srinivasan, B.; Le Tonquesse, S.; Gellé, A.; Bourgès, C.; Monier, L.; Ohkubo, I.; Halet, J. F.; Berthebaud, D.; Mori, T. Screening of Transition (Y, Zr, Hf, V, Nb, Mo, and Ru) and Rare-Earth (La and Pr) Elements as Potential Effective Dopants for Thermoelectric GeTe - an Experimental and Theoretical Appraisal. *J. Mater. Chem. A* **2020**, (38), 19805–19821. https://doi.org/10.1039/d0ta06710e.

(8) Xing, T.; Song, Q.; Qiu, P.; Zhang, Q.; Gu, M.; Xia, X.; Liao, J.; Shi, X.; Chen, L. High Efficiency GeTe-Based Materials and Modules for Thermoelectric Power Generation. *Energy Environ. Sci.* **2021**, *14*, 995–1003. https://doi.org/10.1039/d0ee02791j.

(9) Mao, J.; Zhu, H.; Ding, Z.; Liu, Z.; Gamage, G. A.; Chen, G.; Ren, Z. High Thermoelectric Cooling Performance of *n*-Type Mg_3Bi_2-Based Materials. *Science* **2019**, *365*, 495–498. https://doi.org/10.1126/science.aax7792.

(10) Liu, Z.; Sato, N.; Gao, W.; Yubuta, K.; Kawamoto, N.; Mitome, M.; Kurashima, K.; Owada, Y.; Nagase, K.; Lee, C. H.; Yi, J.; Tsuchiya, K.; Mori, T. Demonstration of Ultrahigh Thermoelectric Efficiency of ~7.3% in Mg_3Sb_2/MgAgSb Module for Low-Temperature Energy Harvesting. *Joule* **2021**, *5*, 1196–1208. https://doi.org/10.1016/j.joule.2021.03.017.

(11) Caballero-Calero, O.; Ares, J. R.; Martín-González, M. Environmentally Friendly Thermoelectric Materials: High Performance from Inorganic Components with Low Toxicity and Abundance in the Earth. *Adv. Sustain. Syst.* **2021**, *5*, 2100095. https://doi.org/10.1002/adsu.202100095.

(12) Zhou, B.; Chen, L.; Li, C.; Qi, N.; Chen, Z.; Su, X.; Tang, X. F. Significant Enhancement in the Thermoelectric Performance of Aluminum-Doped ZnO Tuned by Pore Structure. *ACS Appl. Mater. Interfaces* **2020**, *12*, 51669–51678. https://doi.org/10.1021/acsami.0c16506.

(13) Acharya, S.; Yu, B. K.; Hwang, J.; Kim, J.; Kim, W. High Thermoelectric Performance of ZnO by Coherent Phonon Scattering and Optimized Charge Transport. *Adv. Funct. Mater.* **2021**, *31*, 2105008. https://doi.org/10.1002/adfm.202105008.

(14) Guélou, G.; Lemoine, P.; Raveau, B.; Guilmeau, E. Recent Developments in High-Performance Thermoelectric Sulphides: An Overview of the Promising Synthetic Colusites. *J. Mater. Chem. C* **2021**, *9*, 773–795. https://doi.org/10.1039/d0tc05086e.

(15) Kamińska, P.; Bourgès, C.; Chetty, R.; Gutiérrez-Del-Río, D.; Śpiewak, P.; Święszkowski, W.; Nishimura, T.; Mori, T. Insight into the Preponderant Role of the Lattice Size in Sn-Based Colusites for Promoting a High Power Factor. *J. Mater. Chem. A* **2022**, *10*, 10701–10714. https://doi.org/10.1039/d2ta01210c.

(16) lack, G. A. CRC Handbook of Thermoelectrics, Rowe, D. M.; Ed.; CRC Press: Boca Raton, FL, 1995; Chapter 34, p.407.

(17) O'Brien, R. C.; Ambrosi, R. M.; Bannister, N. P.; Howe, S. D.; Atkinson, H. V. Safe Radioisotope Thermoelectric Generators and Heat Sources for Space Applications. *J. Nucl. Mater.* **2008**, *377*, 506–521. https://doi.org/10.1016/j.jnucmat.2008.04.009.

(18) Prado-Gonjal, J.; Phillips, M.; Vaqueiro, P.; Min, G.; Powell, A. V. Skutterudite Thermoelectric Modules with High Volume-Power-Density: Scalability and Reproducibility. *ACS Appl. Energy Mater.* **2018**, *1*, 6609–6618. https://doi.org/10.1021/acsaem.8b01548.

(19) Rogl, G.; Rogl, P. How Nanoparticles Can Change the Figure of Merit, ZT, and Mechanical Properties of Skutterudites. *Mater. Today Phys.* **2017**, *3*, 48–69. https://doi.org/10.1016/j.mtphys.2017.12.004.

(20) Rull-Bravo, M.; Moure, A.; Fernández, J. F.; Martín-González, M. Skutterudites as Thermoelectric Materials: Revisited. *RSC Adv.* **2015**, *5*, 41653–41667. https://doi.org/10.1039/c5ra03942h.

(21) Rogl, G.; Rogl, P. Skutterudites, a Most Promising Group of Thermoelectric Materials. *Curr. Opin. Green Sustain. Chem.* **2017**, *4*, 50–57. https://doi.org/10.1016/j.cogsc.2017.02.006.

(22) Rogl, G.; Rogl, P. F. Filled Sb-Based Skutterudites from 1996–2022. *Crystals*, **2022**, *12*, 1843. https://doi.org/10.3390/cryst12121843.

(23) Rogl, G.; Ghosh, S.; Renk, O.; Yubuta, K.; Grytsiv, A.; Schafler, E.; Zehetbauer, M.; Mallik, R. C.; Bauer, E.; Rogl, P. Influence of Shear Strain on HPT-Processed *n*-Type Skutterudites Yielding ZT=2.1. *J. Alloys Compd.* **2021**, *855*, 157409. https://doi.org/10.1016/j.jallcom.2020.157409.

(24) He, T.; Calvarese, T. G.; Chen, J.-Z.; Rosenfeld, H. D.; Small, R. J.; Krajewski, J. J.; Subramanian, M. A. Origin of Low Thermal Conductivity in α-Mn: Enhancing the ZT of $YbAl_3$ and $CoSb_3$ through Mn Addition. In *ICT 2005. 24th International Conference on Thermoelectrics, 2005.*; IEEE, **2005**; 434–439. https://doi.org/10.1109/ICT.2005.1519980.

(25) Park, K.-H.; Kim, I.-H. Thermoelectric Properties of $Co_{4-x}Mn_xSb_{12-y}Sn_y$ Skutterudites. *Elec. Mater. Lett.* **2011**, *7*, 39–43. https://doi.org/10.1007/s13391-011-0306-5.

(26) Qiu, P.; Shi, X.; Liu, R.; Qiu, Y.; Wan, S.; Chen, L. Thermoelectric Properties of Manganese-Doped *p*-Type Skutterudites Ce_y $Fe_{4-x}Mn_xSb_{12}$. *Func. Mater. Lett.* **2013**, *06*, 1340003. https://doi.org/10.1142/S1793604713400031.

(27) Ang, R.; Khan, A. U.; Tsujii, N.; Takai, K.; Nakamura, R.; Mori, T. Thermoelectricity Generation and Electron-Magnon Scattering in a Natural Chalcopyrite Mineral from a Deep-Sea Hydrothermal Vent. *Angew. Chem. Int. Ed.* **2015**, *54*, 12909–12913. https://doi.org/10.1002/anie.201505517.

(28) Watzman, S. J.; Duine, R. A.; Tserkovnyak, Y.; Boona, S. R.; Jin, H.; Prakash, A.; Zheng, Y.; Heremans, J. P. Magnon-Drag Thermopower and Nernst Coefficient in Fe, Co, and Ni. *Phys. Rev. B* **2016**, *94*, 144407. https://doi.org/10.1103/PhysRevB.94.144407.

(29) Ahmed, F.; Tsujii, N.; Mori, T. Thermoelectric Properties of $CuGa_{1-x}Mn_xTe_2$: Power Factor Enhancement by Incorporation of Magnetic Ions. *J. Mater. Chem. A* **2017**, *5*, 7545–7554. https://doi.org/10.1039/c6ta11120c.

(30) Polash, M. M. H.; Vashaee, D. Magnon-Bipolar Carrier Drag Thermopower in Antiferromagnetic/Ferromagnetic Semiconductors: Theoretical Formulation and Experimental Evidence. *Phys. Rev. B* **2020**, *102*, 045202. https://doi.org/10.1103/PhysRevB.102.045202.

(31) Matsuura, H.; Ogata, M.; Mori, T.; Bauer, E. Theory of Huge Thermoelectric Effect Based on a Magnon Drag Mechanism: Application to Thin-Film Heusler Alloy. *Phys. Rev. B* **2021**, *104*, 214421. https://doi.org/10.1103/PhysRevB.104.214421.

(32) Koshibae, W.; Maekawa, S. Effects of Spin and Orbital Degeneracy on the Thermopower of Strongly Correlated Systems. *Phys. Rev. Lett.* **2001**, *87*, 236603. https://doi.org/10.1103/PhysRevLett.87.236603.

(33) Hébert, S.; Daou, R.; Maignan, A.; Das, S.; Banerjee, A.; Klein, Y.; Bourgès, C.; Tsujii, N.; Mori, T. Thermoelectric Materials Taking Advantage of Spin Entropy: Lessons from Chalcogenides and Oxides. *Sci. Technol. Adv. Mater.* **2021**, *22*, 583–596. https://doi.org/10.1080/14686996.2021.1951593.

(34) Zhang, J.; Tse, K.; Wong, M.; Zhang, Y.; Zhu, J. A Brief Review of Co-Doping. *Front. Phys*., **2016**, *11*, 117405. https://doi.org/10.1007/s11467-016-0577-2.

(35) Liu, W.-S.; Zhang, B.-P.; Zhao, L.-D.; Li, J.-F. Improvement of Thermoelectric Performance of $CoSb_{3-x}Te_x$ Skutterudite Compounds by Additional Substitution of IVB-Group Elements for Sb. *Chem. Mater.* **2008**, *20*, 7526–7531. https://doi.org/10.1021/cm802367f.

(36) Nagamoto, Y.; Tanaka, K.; Koyanagi, T. Transport Properties of Heavily Doped N-Type $CoSb_3$. In *Seventeenth International Conference on Thermoelectrics. Proceedings ICT98*; IEEE, **1998**; 302–305. https://doi.org/10.1109/ICT.1998.740378.

(37) Li, X. Y.; Chen, L. D.; Fan, J. F.; Zhang, W. B.; Kawahara, T.; Hirai, T. Thermoelectric Properties of Te-Doped $CoSb_3$ by Spark Plasma Sintering. *J. Appl. Phys.* **2005**, *98*, 083702. https://doi.org/10.1063/1.2067704.

(38) Kobayashi, K.; Khan, A. U.; Mori, T. Electronic Structures of Si- and Te-Doped $CoSb_3$ Compounds under High Pressures. *Jpn. J. Appl. Phys.* **2017**, *56*, 05FB07. https://doi.org/10.7567/JJAP.56.05FB07.

(39) Khan, A. U.; Kobayashi, K.; Tang, D. M.; Yamauchi, Y.; Hasegawa, K.; Mitome, M.; Xue, Y.; Jiang, B.; Tsuchiya, K.; Golberg, D.; Bando, Y.; Mori, T. Nano-Micro-Porous Skutterudites with

100% Enhancement in ZT for High Performance Thermoelectricity. *Nano Energy* **2017**, *31*, 152–159. https://doi.org/10.1016/j.nanoen.2016.11.016.

(40) Liang, T.; Su, X.; Yan, Y.; Zheng, G.; She, X.; You, Y.; Uher, C.; Kanatzidis, M. G.; Tang, X. Panoscopic Approach for High-Performance Te-Doped Skutterudite. *NPG Asia Mater.* **2017**, *9*, e352. https://doi.org/10.1038/am.2017.1.

(41) Bourgès, C.; Sato, N.; Baba, T.; Baba, T.; Ohkubo, I.; Tsujii, N.; Mori, T. Drastic Power Factor Improvement by Te Doping of Rare Earth-Free $CoSb_3$-Skutterudite Thin Films. *RSC Adv.* **2020**, *10*, 21129–21135. https://doi.org/10.1039/d0ra02699a.

(42) Kato, A.; Bourgès, C.; Pang, H.; Gutiérrez, D.; Sakurai, T.; Mori, T. Facile Fabrication of N-Type Flexible $CoSb_{3-x}Te_x$ Skutterudite/PEDOT:PSS Hybrid Thermoelectric Films. *Polymers* **2022**, *14*, 1986. https://doi.org/10.3390/polym14101986.

(43) Lei, Y.; Gao, W.; Zheng, R.; Li, Y.; Chen, W.; Zhang, L.; Wan, R.; Zhou, H.; Liu, Z.; Chu, P. K. Ultrafast Synthesis of Te-Doped $CoSb_3$ with Excellent Thermoelectric Properties. *ACS Appl. Energy Mater.* **2019**, *2*, 4477–4485. https://doi.org/10.1021/acsaem.9b00720.

(44) Rodríguez-Carvajal, J. Recent Advances in Magnetic Structure Determination by Neutron Powder Diffraction. *Physica B Condens. Matter.* **1993**, *192*, 55–69. https://doi.org/10.1016/0921-4526(93)90108-I.

(45) Roisnel, T.; Rodríguez-Carvajal, J. WinPLOTR: A Windows Tool for Powder Diffraction Pattern Analysis. In *Mater. Sci. Forum*; **2001**; *378–381*, 118–123. https://doi.org/10.4028/www.scientific.net/msf.378-381.118.

(46) Alleno, E.; Bérardan, D.; Byl, C.; Candolfi, C.; Daou, R.; Decourt, R.; Guilmeau, E.; Hébert, S.; Hejtmanek, J.; Lenoir, B.; Masschelein, P.; Ohorodnichuk, V.; Pollet, M.; Populoh, S.; Ravot, D.; Rouleau, O.; Soulier, M. Invited Article: A Round Robin Test of the Uncertainty on the Measurement of the Thermoelectric Dimensionless Figure of Merit of $Co_{0.97}Ni_{0.03}Sb_3$. *Rev. Sci. Instr.* **2015**, *86*, 011301. https://doi.org/10.1063/1.4905250.

(47) Giannozzi, P.; Baroni, S.; Bonini, N.; Calandra, M.; Car, R.; Cavazzoni, C.; Ceresoli, D.; Chiarotti, G. L.; Cococcioni, M.; Dabo, I.; Dal Corso, A.; de Gironcoli, S.; Fabris, S.; Fratesi, G.; Gebauer, R.; Gerstmann, U.; Gougoussis, C.; Kokalj, A.; Lazzeri, M.; Martin-Samos, L.; Marzari, N.; Mauri, F.; Mazzarello, R.; Paolini, S.; Pasquarello, A.; Paulatto, L.; Sbraccia, C.; Scandolo, S.; Sclauzero, G.; Seitsonen, A. P.; Smogunov, A.; Umari, P.; Wentzcovitch, R. M. QUANTUM ESPRESSO: A Modular and Open-Source Software Project for Quantum Simulations of Materials. *J. Phys. Cond. Matter.* **2009**, *21*, 395502. https://doi.org/10.1088/0953-8984/21/39/395502.

(48) Perdew, J. P.; Burke, K.; Ernzerhof, M. Generalized Gradient Approximation Made Simple. *Phys. Rev. Lett.* **1996**, *77*, 3865–3868. https://doi.org/10.1103/PhysRevLett.77.3865.

(49) Blöchl, P. E. Projector Augmented-Wave Method. *Phys. Rev. B* **1994**, *50*, 17953–17979. https://doi.org/10.1103/PhysRevB.50.17953.

(50) Kresse, G.; Joubert, D. From Ultrasoft Pseudopotentials to the Projector Augmented-Wave Method. *Phys. Rev. B* **1999**, *59*, 1758–1775. https://doi.org/10.1103/PhysRevB.59.1758.

(51) Li, G.; Bajaj, S.; Aydemir, U.; Hao, S.; Xiao, H.; Goddard, W. A.; Zhai, P.; Zhang, Q.; Snyder, G. J. P-Type Co Interstitial Defects in Thermoelectric Skutterudite $CoSb_3$ Due to the Breakage of Sb_4-Rings. *Chem. Mater.* **2016**, *28*, 2172–2179. https://doi.org/10.1021/acs.chemmater.6b00112.

(52) Park, C. H.; Kim, Y. S. Ab Initio Study of Native Point-Defects in $CoSb_3$: Understanding off-Stoichiometric Doping Properties. *Phys. Rev. B* **2010**, *81*, 085206. https://doi.org/10.1103/PhysRevB.81.085206.

(53) Li, G.; Aydemir, U.; Wood, M.; Goddard, W. A.; Zhai, P.; Zhang, Q.; Snyder, G. J. Defect-Controlled Electronic Structure and Phase Stability in Thermoelectric Skutterudite $CoSb_3$. *Chem. Mater.* **2017**, *29*, 3999–4007. https://doi.org/10.1021/acs.chemmater.7b00559.

(54) Kuwabara, A.; Tanaka, I. First Principles Calculation of Defect Formation Energies in Sr- and Mg-Doped $LaGaO_3$. *J. Phys. Chem. B* **2004**, *108*, 9168–9172. https://doi.org/10.1021/jp049808m.

(55) Freysoldt, C.; Neugebauer, J.; Van De Walle, C. G. Fully Ab Initio Finite-Size Corrections for Charged-Defect Supercell Calculations. *Phys. Rev. Lett.* **2009**, *102*, 016402. https://doi.org/10.1103/PhysRevLett.102.016402.

(56) Anand, S.; Toriyama, M. Y.; Wolverton, C.; Haile, S. M.; Snyder, G. J. A Convergent Understanding of Charged Defects. *Acc. Mater. Res.* **2022**, *3*, 685–696. https://doi.org/10.1021/accountsmr.2c00044.

(57) Tang, Y.; Gibbs, Z. M.; Agapito, L. A.; Li, G.; Kim, H. S.; Nardelli, M. B.; Curtarolo, S.; Snyder, G. J. Convergence of Multi-Valley Bands as the Electronic Origin of High Thermoelectric Performance in $CoSb_3$ Skutterudites. *Nat. Mater.* **2015**, *14*, 1223–1228. https://doi.org/10.1038/nmat4430.

(58) Hanus, R.; Guo, X.; Tang, Y.; Li, G.; Snyder, G. J.; Zeier, W. G. A Chemical Understanding of the Band Convergence in Thermoelectric $CoSb_3$ Skutterudites: Influence of Electron Population, Local Thermal Expansion, and Bonding Interactions. *Chem. Mater.* **2017**, *29*, 1156–1164. https://doi.org/10.1021/acs.chemmater.6b04506.

(59) Luo, H.; Krizan, J. W.; Muechler, L.; Haldolaarachchige, N.; Klimczuk, T.; Xie, W.; Fuccillo, M. K.; Felser, C.; Cava, R. J. A Large Family of Filled Skutterudites Stabilized by Electron Count. *Nat. Commun.* **2015**, *6*, 6489. https://doi.org/10.1038/ncomms7489.

(60) Yang, J.; Endres, M. G.; Meisner, G. P. Valence of Cr in Skutterudites: Electrical Transport and Magnetic Properties of Cr-Doped $CoSb_3$. *Phys. Rev. B* **2002**, *66*, 014436. https://doi.org/10.1103/PhysRevB.66.014436.

(61) Cutler, M.; Mott, N. F. Observation of Anderson Localization in an Electron Gas. *Phys. Rev.* **1969**, *181*, 1336–1340. https://doi.org/10.1103/PhysRev.181.1336.

(62) Snyder, G. J.; Snyder, A. H.; Wood, M.; Gurunathan, R.; Snyder, B. H.; Niu, C. Weighted Mobility. *Adv. Mater.* **2020**, *32*, 2001537. https://doi.org/10.1002/adma.202001537.

(63) Zheng, Y.; Lu, T.; Polash, M. H.; Rasoulianboroujeni, M.; Liu, N.; Manley, M. E.; Deng, Y.; Sun, P. J.; Chen, X. L.; Hermann, R. P.; Vashaee, D.; Heremans, J. P.; Zhao, H. Paramagnon Drag in High Thermoelectric Figure of Merit Li-Doped MnTe. *Sci. Adv.* **2019**, *5*, eaat9461. https://doi.org/10.1126/sciadv.aat9461.

(64) Chevalier, P. Y.; Fischer-, E.; Marbeuf, A. A Thermodynamic Evaluation of the Mn-Te Binary System. *Thermochim. Acta* **1993**, *223*, 51–63. https://doi.org/10.1016/0040-6031(93)80119-U.

(65) Pei, Y.; Gibbs, Z. M.; Gloskovskii, A.; Balke, B.; Zeier, W. G.; Snyder, G. J. Optimum Carrier Concentration in N-Type PbTe Thermoelectrics. *Adv. Energy Mater.* **2014**, *4*, 1400486. https://doi.org/10.1002/aenm.201400486.

(66) Gayner, C.; Amouyal, Y. Energy Filtering of Charge Carriers: Current Trends, Challenges, and Prospects for Thermoelectric Materials. *Adv. Funct. Mater.* **2020**, *30*, 1901789. https://doi.org/10.1002/adfm.201901789.

(67) Pakdel, A.; Guo, Q.; Nicolosi, V.; Mori, T. Enhanced Thermoelectric Performance of Bi-Sb-Te/Sb_2O_3 Nanocomposites by Energy Filtering Effect. *J. Mater. Chem. A* **2018**, *6*, 21341–21349. https://doi.org/10.1039/c8ta08238c.

(68) Tsujii, N.; Nishide, A.; Hayakawa, J.; Mori, T. Observation of Enhanced Thermopower Due to Spin Fluctuation in Weak Itinerant Ferromagnet. *Sci. Adv.* **2019**, *5*, eaat5935. https://doi.org/10.1126/sciadv.aat5935.

(69) Takaki, H.; Kobayashi, K.; Shimono, M.; Kobayashi, N.; Hirose, K.; Tsujii, N.; Mori, T. Thermoelectric Properties of a Magnetic Semiconductor $CuFeS_2$. *Mater. Today Phys.* **2017**, *3*, 85–92. https://doi.org/10.1016/j.mtphys.2017.12.006.

(70) Dalal, V. N. K.; Prabhu, R. B. Electrical Resistivity and Magnetic Susceptibility of Antiferromagnetic MnTe. *Physica B+C* **1982**, *112*, 42–44. https://doi.org/10.1016/0378-4363(82)90127-9.